Physics and modeling of trailing-edge stall phenomena for wall-modeled large-eddy simulation

Yoshiharu Tamaki ,* Yuma Fukushima , Yuichi Kuya , and Soshi Kawai
Department of Aerospace Engineering, Tohoku University, Sendai, Miyagi 980-8579, Japan

(Received 30 September 2019; accepted 4 June 2020; published 6 July 2020; corrected 14 April 2021)

The wall-resolved large-eddy simulation (WRLES) database of the flow around the A-airfoil at the near-stall condition [K. Asada and S. Kawai, Phys. Fluids **30**, 085103 (2018)] is analyzed to understand the mechanism of the boundary layer development and to examine the predictability of the trailing-edge stall phenomena using the wall-modeled LES (WMLES). The analysis based on the integral relation for the boundary layer indicates that the skin friction has dominant effects on the boundary layer development in the mild-adverse pressure gradient region ($x/c > 0.6$). The effects of the skin friction accumulate along the airfoil upper surface, which determines the growth of the momentum thickness in the downstream and the consequent flow separation near the trailing edge. Therefore, this analysis indicates that the wall modeling in $x/c < 0.6$ is important for the prediction of the stall phenomena, while that near and downstream of the separation location little affects the stall phenomena. Also, the budget analysis reveals that the eddy viscosity in the mild-adverse pressure gradient regions increases compared to that of the equilibrium boundary layer, which should be incorporated properly in the wall model. The same flowfield is simulated using the WMLES, and the results show an overall good agreement with the WRLES. The analysis based on the integral relation indicates that the WMLES can predict the stall phenomena with reasonable accuracy because the outer layer turbulence, whose effects are dominant near the separation point, is directly resolved in the WMLES. Despite the overall agreement with the WRLES, the WMLES results also suggest that potential issues remain in the underresolution near the leading edge and the eddy viscosity modeling of the wall model for flows with adverse pressure gradient.

DOI: 10.1103/PhysRevFluids.5.074602

I. INTRODUCTION

Predicting stall characteristics is critical in aerodynamic designing of aircraft because the stall characteristics determine the performance of the aircraft at takeoff and landing conditions. The stall phenomena can be categorized into the following three types: trailing-edge stall, leading-edge stall, and the thin-airfoil stall [1,2]. In the trailing-edge stall flowfield, flow separation occurs near the trailing edge, whose location moves upstream as the angle of attack increases. The trailing-edge stall is assumed to be the most favorable in airfoil design among the three types of the stall phenomena because the change of the lift force near the maximum lift point is gradual compared to the other stall types, and accurate prediction of this stall phenomena is therefore desired. In the trailing-edge stall flowfield, the boundary layer is subjected to the relatively gradual adverse pressure gradient, which finally leads to the separation near the trailing edge. Thus, the effects of the adverse pressure gradient in the boundary layer development must be correctly evaluated to predict the trailing-edge stall phenomena in numerical simulations.

*tamaki@klab.mech.tohoku.ac.jp

Recently, large-eddy simulation (LES) is becoming feasible due to the growth of computational resources. LES is expected to be a promising method to understand the flow physics of the stall phenomena because the model dependency of LES is much smaller than that of simulations using the Reynolds-averaged Navier-Stokes (RANS) equations. For example, near-stall flowfield around the Aerospatiale A-airfoil at $\mathrm{Re}_c = 2.1 \times 10^6$ (Re_c is the Reynolds number based on the mean aerodynamic chord length and the free-stream velocity) was simulated in the LESFOIL project [3]. Asada and Kawai [4] also conducted LES of the A-airfoil case using the state-of-the-art supercomputer (their detailed data are available at the website [5]). They checked convergences obtained about the grid resolution and the spanwise extent in their largest simulation case (approximately 1 billion grid points with a spanwise extent of 5% chord). However, as noted by previous researchers [6,7], the computational cost of LES becomes prohibitively large at higher Reynolds numbers, which makes flow simulations at the full-aircraft-scale Reynolds number ($\mathrm{Re}_c \sim 10^7$) not realistic.

To reduce the computational cost of the LES at high Reynolds numbers, wall-modeled LES (WMLES; see review articles [8–10]) is attracting attention. WMLES can be classified into several approaches; for example, the hybrid LES-RANS approach (e.g., the improved detached-eddy simulations [11], the wall-stress approach [12–17], the off-wall boundary condition approach [18], and the dynamic-slip approach [19,20]). In these WMLES approaches, only the inner layer of the boundary layer is modeled, while the unsteady flow motions in the outer layer are directly resolved by the grid. The augmentation of the computational cost of the LES by the increase of the Reynolds number mostly depends on the reduction of the inner-layer length scale [6,7], and thus the use of wall model can avoid the rapid increase of the computational cost. However, these wall models are generally derived by similarity laws near the wall, which may introduce uncertainty to simulations of complex flows. The equilibrium wall models (e.g., Ref. [14]) assume an equilibrium state of the boundary layer; i.e., the unsteady, convection, and pressure gradient terms are neglected in the modeling. In addition to the equilibrium wall models, the nonequilibrium wall models [13,15–17,21] have also been studied, which solves RANS-type equations including the unsteady, convection and pressure gradient terms to incorporate the nonequilibrium effects. Although the nonequilibrium wall models are expected to be more suitable for flows with a pressure gradient than the equilibrium wall models, additional difficulties exist in the modeling. Some of the nonequilibrium wall models neglect the convection or time-derivative terms [13,16], although Wang and Moin [13] and Hickel *et al.* [22] reported that the balances of the three (the time-derivative, convection, and pressure gradient) terms are important in the prediction of flow separation and that neglecting one of them is physically inconsistent. Kawai and Larsson [15] also showed that the convection term in the wall model creates resolved Reynolds stress, and the modeled eddy viscosity must be reduced accordingly. Since even the nonequilibrium wall models include the assumptions stated above, the validity of the wall models for the flows with pressure gradient is not clear.

The WMLES has been validated in the simulations of separated flows: for example, flows over a hill or hump [23–26], airfoil flowfields at a high-angle of attack [15,25], and full-aircraft flowfields [27]. Park [26] reported that the nonequilibrium wall models can reproduce more accurate skin friction distributions than the equilibrium wall models. On the other hand, some researchers reported that WMLES with even the equilibrium wall models can reproduce the separated flows induced by gradual adverse pressure gradient [24,25] with reasonable accuracy. Also, concerning the shock-induced flow separation, Kawai and Larsson [28] and Bermejo-Moreno *et al.* [29] showed that the velocity distributions obtained by the WMLES using an equilibrium model shows good agreement with the experimental data. Fukushima and Kawai [30] simulated the transonic buffet phenomenon occurring on a supercritical airfoil using an equilibrium wall model and showed that the shock oscillating phenomena are well predicted compared to the experimental measurements. To summarize these studies, we must separately consider the accuracy of the flowfield predicted by the LES and that of the skin friction because the wall model (in the wall-stress approach) determines only the skin friction imposed as the wall boundary flux of the LES. Therefore, we must clarify the relationship between the skin friction imposed by the wall model and the LES flowfield to discuss the predictability of the separated flow by the WMLES.

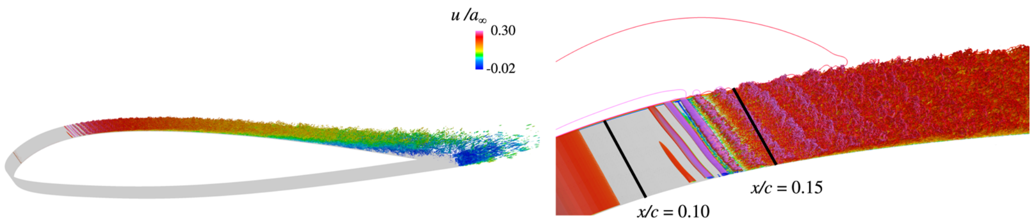

FIG. 1. Overview of the WRLES flowfield around A-airfoil at the near-stall condition (isosurfaces of the Q criterion colored by the streamwise velocity, reproduced from Ref. [4]).

The objective of this paper is to understand the predictability of the trailing-edge stall phenomena using WMLES. For this purpose, we will investigate the following two points separately:

(i) effects of the skin friction calculated by the wall models to the boundary layer development in the LES and

(ii) accuracy of the skin friction predicted by the wall models in the flows with a pressure gradient.

To clarify these key points, we first analyze the prior WRLES database of the near-stall airfoil flow [4,5] in Sec. II. Here the effects of the skin friction on the development of the boundary layer are evaluated based on the analysis using the integral relation [31]. Also, the nonequilibrium effects in the boundary layer are investigated through the budget analysis to understand the validity and necessity of the nonequilibrium wall models. Then, to validate the observations from the WRLES and discuss the predictability of the stall phenomena by WMLES, WMLES computations of the same flowfield as the WRLES are conducted using the equilibrium-nonequilibrium wall models [14,15] in Sec. III.

II. ANALYSIS OF NEAR-STALL FLOW WALL-RESOLVED LES DATABASE

In this section, we analyze the WRLES database of the flowfield around the Aerospatiale A-airfoil at a near-stall condition [4,5]. Specifically, we investigate the following two points:

(i) contributions of the skin friction to the boundary layer development and

(ii) nonequilibrium effects of the boundary layer at the adverse pressure gradient locations.

In the WRLES database, the Reynolds number based on the chord length c and the free-stream velocity U_∞ is 2.1×10^6, the angle of attack $\alpha = 13.3^\circ$, and the free-stream Mach number is 0.15. In this simulation, the grid spacings in the wall-parallel and spanwise directions are set to smaller than 25 and 13 in the wall unit, respectively, which are sufficiently small to resolve the near-wall streak structure [32]. The sixth-order compact difference scheme [33] is used to evaluate the spatial derivatives, and the second-order implicit time integration method [34,35] is used to evaluate the time advancement. In the WRLES, the subgrid-scale (SGS) turbulence model is not used explicitly to model the SGS terms. Instead, the 10th-order compact low-pass filtering method [36] is used to introduce SGS-like dissipation. In the following, the wall-parallel and -normal coordinates are defined as ξ and η, respectively, while the coordinate in the airfoil chord direction is denoted as x.

The overview of the flowfield obtained by the WRLES [4] is shown in Fig. 1. The laminar flow near the leading edge separates and creates a laminar-separation bubble. This laminar-separation bubble induces the flow instability, and then laminar-turbulence transition occurs at $x/c \approx 0.14$. The turbulent boundary layer grows along the airfoil, and turbulent flow separation is observed near the trailing edge ($x/c \approx 0.8$). The prediction of the turbulent flow separation is critical in the prediction of the stall phenomena because the separation near the trailing edge changes the circulation around the airfoil. In this paper, we focus on the prediction of the mean flowfield, and thus, we analyze the spanwise- and time-averaged quantities of the WRLES flowfield.

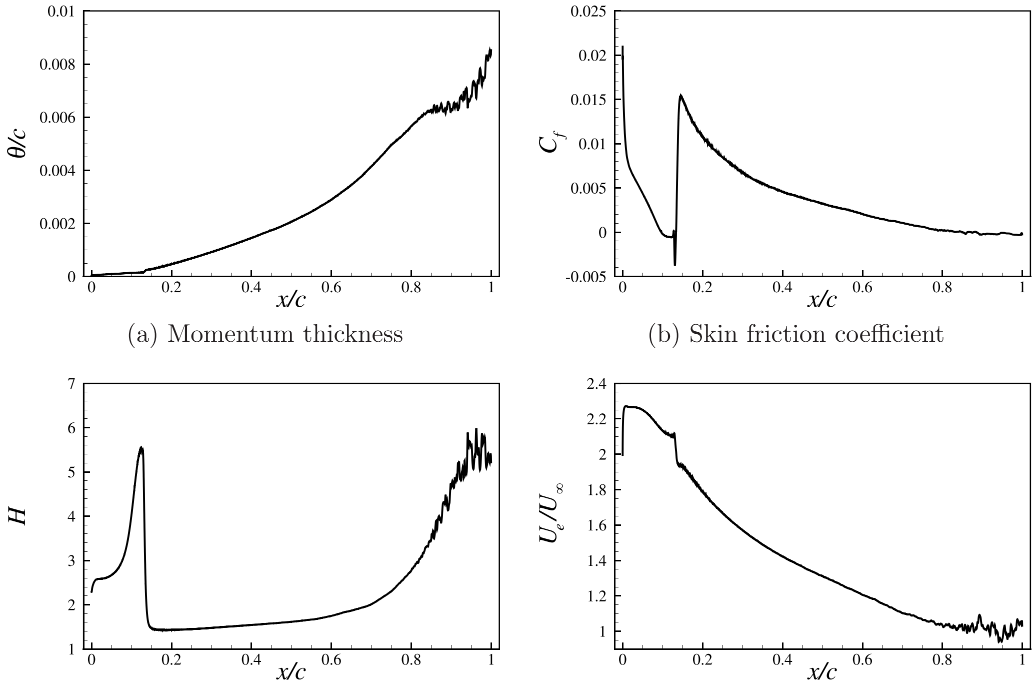

(a) Momentum thickness (b) Skin friction coefficient

(c) Shape factor (d) Velocity at boundary-layer edge

FIG. 2. Statistical quantities of the boundary layer along the airfoil upper surface obtained by the WRLES (reproduced from Ref. [4]).

A. Contribution of the skin friction to the boundary layer development

To predict the airfoil stall phenomena, the boundary layer development along the airfoil must be predicted accurately. This is because the displacement by the boundary layer changes the circulation around the airfoil, and, generally, the lift decreases from the inviscid condition as the consequence. To discuss the validity of the WMLES, we have to clarify where the skin friction is effective to the boundary layer development compared to the other effects (i.e., acceleration or deceleration of the outer flowfield). Therefore, we introduce the integral relation [31]:

$$\frac{d\theta}{d\xi} = I + II, \quad I \equiv \frac{C_f^*}{2},\ II \equiv -(2+H)\frac{\theta}{U_e}\frac{dU_e}{d\xi}, \tag{1}$$

where θ is the momentum thickness, $C_f^* \equiv \tau_w/(\rho_\infty U_e^2) = C_f(U_\infty/U_e)^2$, C_f is skin friction coefficient, $H \equiv \delta^*/\theta$ (δ^*: mass displacement thickness) is the shape factor, τ_w is the skin friction, and U_e is the velocity at the outer edge of the boundary layer. Equation (1) indicates that the spatial development of θ is constituted by the two terms I and II. Here I denotes the contribution of the skin friction, and II is the effects of the acceleration or deceleration of the flow outside the boundary layer. The integral relation [Eq. (1)] is classically used to predict the boundary layer thickness in the inviscid-viscous interaction methods (e.g., XFOIL [37]). In this paper, instead, we substitute the WRLES data to the right-hand side of Eq. (1) to evaluate the contributions of I and II to the development of θ. Figure 2 shows the distribution of the quantities used to calculate the right-hand side of Eq. (1). The previous study [4] indicated that the spanwise domain size of their calculation (4.93% of the chord length) is large enough to eliminate the spanwise correlation and grid resolution is sufficient to achieve the grid converged solution of these ensemble-averaged quantities. Note that θ and δ^* are calculated based on the vorticity-based velocity [38] to eliminate the ambiguity of the

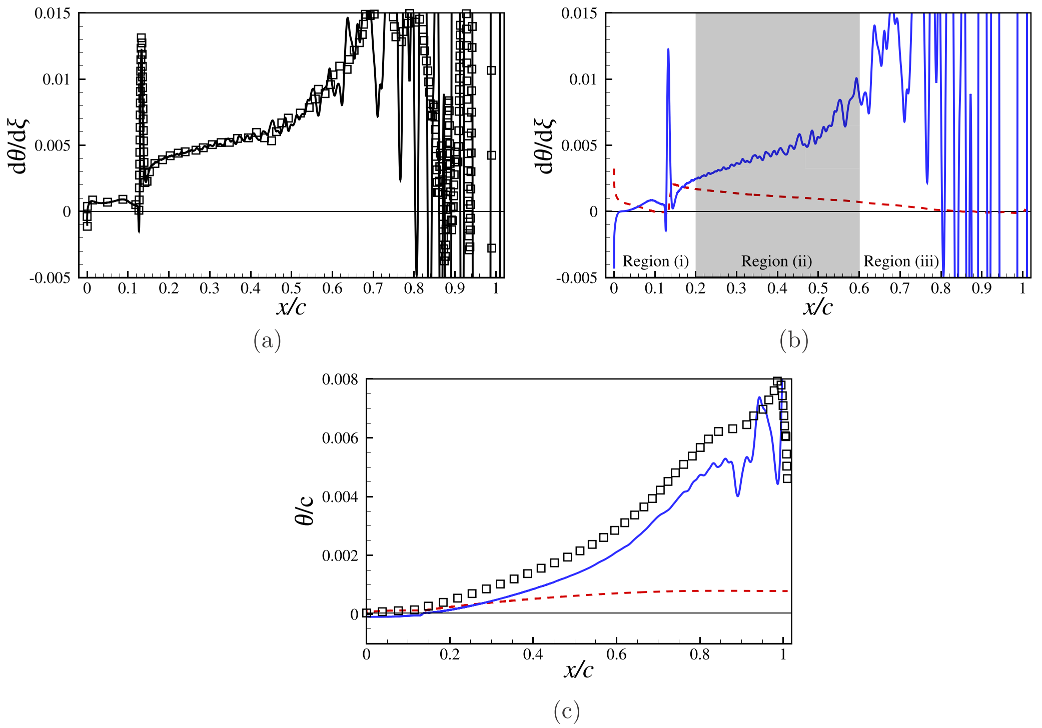

FIG. 3. Integral relation for the boundary layer. (a) Validity of Eq. (1) (□, left-hand side; ——, right-hand side); (b) components of the right-hand side of Eq. (1) (- - -, I; ——, II); (c) term-by-term integrals [Eq. (2). - - -, integral of I; ——, integral of II; □, θ].

boundary layer thickness due to the acceleration or deceleration of the flow outside of the boundary layer, and thus the distributions of θ and H are slightly different from those presented in the previous study [4].

First, to validate Eq. (1), Fig. 3(a) compares $I + II$ to the left-hand side of Eq. (1) that is directly calculated by numerically differentiating θ. Here the result shows the integral relation itself is highly accurate in this flowfield, which suggests that the boundary layer can reasonably be treated by the thin-layer theory. Next, the term-by-term contributions of the right-hand side of Eq. (1) are investigated. Figure 3(b) shows the distribution of I and II along the airfoil upper surface. For the discussion below, the flowfield is divided into the following three regions:

(1) laminar or transitional region ($x/c < 0.2$),

(2) mild-adverse pressure gradient region ($0.2 < x/c < 0.6$), and

(3) strong adverse pressure gradient or separated region ($x/c > 0.6$).

In region (i), I is dominant near the leading edge, and then II increases in the separation bubble and the subsequent laminar-turbulent transition region. In region (ii), I and II has a similar magnitude at $x/c \approx 0.2$, and II increases in the downstream. This is because C_f decreases, and the increased θ enhances II further. In region (iii), II is dominant, which implies the effects of the skin friction to the boundary layer development is almost negligible. Although II shows oscillatory distributions in the separated region due to the nonsmooth θ in the separated region, by the definition, I disappears at the separation point, and II becomes dominant.

The integral relation indicates that the skin friction in region (i) and (ii) is responsible for the prediction of the turbulent flow separation in region (iii). This idea becomes clearer by integrating Eq. (1) in ξ direction from the leading edge ($\xi = 0$) to a location along the upper surface of the airfoil ($\xi = \xi_1$) as

$$\theta(\xi_1) = \int_0^{\xi_1} I d\xi + \int_0^{\xi_1} II d\xi. \tag{2}$$

Figure 3(c) shows the terms of Eq. (2). At $x/c = 0.8$, approximately 15% of θ is due to the upstream I term. Since I in regions (i) and (ii) has nonnegligible contributions to the development of θ, the prediction of the skin friction in regions (i) and (ii) consequently affects θ in region (iii). Also, since II term includes θ itself, the growth rate of θ is affected by θ itself at the location especially where II is dominant [i.e., region (iii)]. Therefore, if the θ at some location is underestimated, the growth rate of θ is also underestimated throughout the downstream boundary layer. This suggests that the skin friction in the upstream locations [regions (i) and (ii)] is important to predict the boundary layer development in region (iii).

In WMLES based on the wall-stress approach, I is imposed by the wall model, while the flow physics related to II (i.e, the outer-layer turbulence) are directly resolved by the grid. The prediction of II is therefore depending almost only on whether θ at that location is accurately obtained. Thus, we must consider the accuracy of the wall model in the relatively mild-pressure gradient region [regions (i) and (ii)], which consequently affects the θ value in region (iii). On the other hand, the contribution of I is almost negligible in region (iii), which implies that an accurate wall modeling is not necessarily required near and downstream of the separation location.

B. Nonequilibrium effects in the boundary layer

Here the inner layer of the boundary layer is analyzed through the budget analysis of the wall-parallel momentum equation similarly to the previous studies [4,22] to obtain insights for the nonequilibrium wall models. In this subsection, we concentrate on the turbulent region [region (ii)]. Note that the laminar part [the former half of region (i)] also has some influences on the downstream boundary layer, which will be discussed in Sec. III B through the WMLES. The budget analysis is based on the Favre-averaged wall-parallel momentum equation:

$$\frac{\partial \overline{\rho}\tilde{U}}{\partial t} + \frac{\partial \overline{\rho}\tilde{U}\tilde{U} + \overline{p}}{\partial \xi} + \frac{\partial \overline{\rho}\tilde{U}\tilde{V}}{\partial \eta} = \frac{\partial (\overline{\tau_{\xi\xi}} - \overline{\rho}\widetilde{U''U''})}{\partial \xi} + \frac{\partial (\overline{\tau_{\xi\eta}} - \overline{\rho}\widetilde{U''V''})}{\partial \eta} + \overline{\mathcal{F}}, \tag{3}$$

where U and V are the wall-parallel and wall-normal velocities, respectively;

$$\tau_{\xi\xi} \equiv \mu\left(\frac{4}{3}\frac{\partial U}{\partial \xi} - \frac{2}{3}\frac{\partial V}{\partial \eta}\right), \ \tau_{\xi\eta} \equiv \mu\left(\frac{\partial U}{\partial \eta} + \frac{\partial V}{\partial \xi}\right),$$

is the viscous stress; and $\mathcal{F}$ is the contribution of the low-pass filtering. Here the Favre averaging for a variable a is defined as $\tilde{a} \equiv \overline{\rho a}/\overline{\rho}$, and the fluctuations as $a'' \equiv a - \tilde{a}$. Note that the effects of the wall curvature are neglected in Eq. (3). Equation (3) is rewritten into the following form to see the contributions of the primary terms:

$$C + P + V + R = \text{(residual)}, \tag{4}$$

where C (convection), P (pressure gradient), V (viscous stress), R (Reynolds stress), and the residual terms are

$$C \equiv -\frac{\partial \overline{\rho}\tilde{U}\tilde{U}}{\partial \xi} - \frac{\partial \overline{\rho}\tilde{U}\tilde{V}}{\partial \eta}, \quad P \equiv -\frac{\partial \overline{p}}{\partial \xi}, \quad V \equiv \frac{\partial \overline{\tau_{\xi\eta}}}{\partial \eta}, \quad R \equiv -\frac{\partial \overline{\rho}\widetilde{U''V''}}{\partial \eta},$$

$$\text{(residual)} \equiv \frac{\partial \overline{\rho}\tilde{U}}{\partial t} - \frac{\partial (\overline{\tau_{\xi\xi}} - \overline{\rho}\widetilde{U''U''})}{\partial \xi} - \overline{\mathcal{F}}.$$

We examine two different locations $x/c = 0.3$ and 0.6 to evaluate the effects of the adverse pressure gradient. Figures 4(a) and 4(b) show the terms of Eq. (4), where the nonequilibrium terms

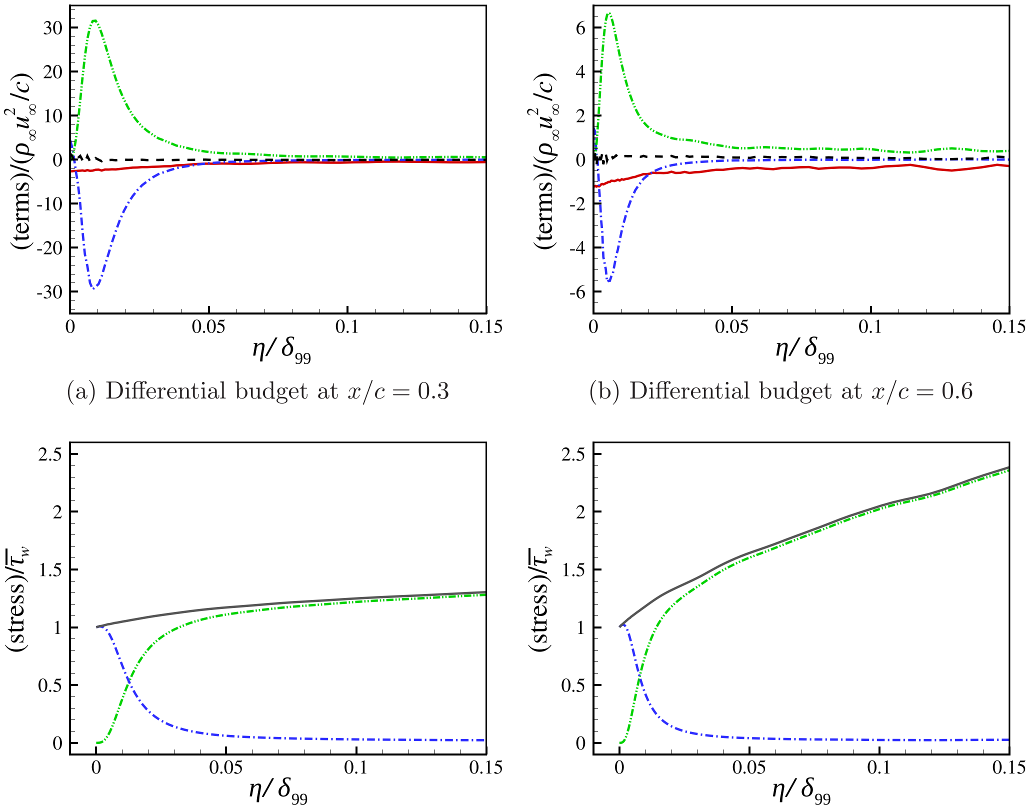

(a) Differential budget at $x/c = 0.3$

(b) Differential budget at $x/c = 0.6$

(c) Integrated budget at $x/c = 0.3$

(d) Integrated budget at $x/c = 0.6$

FIG. 4. Budget of the wall-parallel momentum equation (——, nonequilibrium terms $C + P$; -·-·-·, viscous stress term V; -··-··-, Reynolds stress term R; - - -, residual). For the integrated budget [(c) and (d)], the total shear stress $\mathcal{T}_{\xi\eta}$ (——) is also shown.

(C and P) are plotted as their sum $C + P$ to see the balance between C and P. Note that the residual term is calculated by subtracting C, P, V, and R from zero. The residual term is negligible throughout the boundary layer, and the terms $C + P$, V, and R are balanced. At $x/c = 0.3$, the $C + P$ term shows a small contribution compared to the other two terms, and thus the boundary layer is almost at the equilibrium state. However, the $C + P$ term has a nonnegligible contribution at $x/c = 0.6$ even at the upper bound of the inner layer ($y \sim 0.1\delta_{99}$). This result is in agreement with the observation presented by Hickel *et al.* [22]. The nonequilibrium effects are clearly seen when Eq. (4) is integrated into the wall-normal direction. Integrating Eq. (4) from the wall ($\eta = 0$) to a certain height ($\eta = h$) yields

$$\mathcal{T}_{\xi\eta}(h) = \overline{\tau}_w - \int_0^h (C + P)d\eta, \tag{5}$$

where the residual term is omitted. Also we define the total shear stress as

$$\mathcal{T}_{\xi\eta} \equiv \overline{\tau_{\xi\eta}} - \overline{\rho}\widetilde{U''V''}. \tag{6}$$

In an equilibrium boundary layer, the total shear stress is equal to $\overline{\tau_w}$ because $C + P$ is zero. Figures 4(c) and 4(d) show the profiles of shear stress components in Eq. (6) at $x/c = 0.3$ and $x/c = 0.6$. At $x/c = 0.3$, the equilibrium assumption ($\mathcal{T}_{\xi\eta}/\overline{\tau_w} \approx 1$) is mostly valid throughout the inner layer ($\eta < 0.1\delta_{99}$). On the other hand, the total shear stress at $x/c = 0.6$ increases to $2\overline{\tau_w}$ at

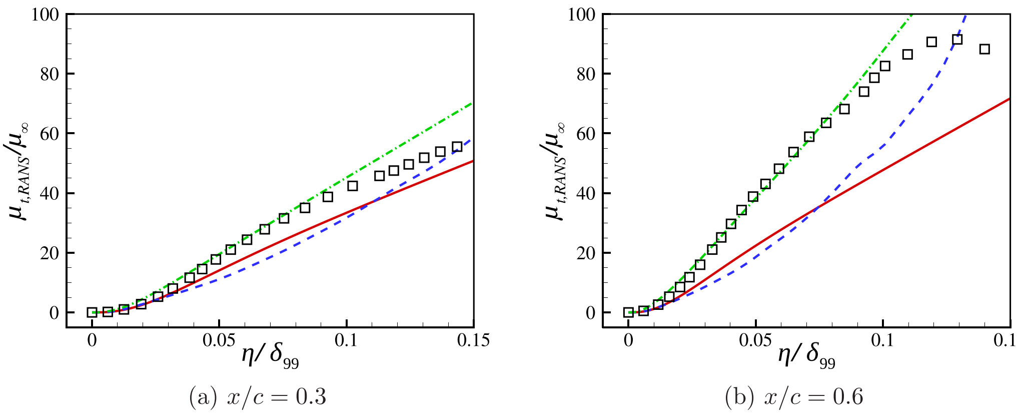

FIG. 5. Comparisons of the RANS eddy viscosity estimations [——, Eq. (8); - - -, Eq. (9); -··-··, Eq. (10); □, effective RANS eddy viscosity, Eq. (11), calculated by the WRLES data].

$\eta = 0.1\delta_{99}$ due to the nonequilibrium effects. Therefore, assuming the equilibrium assumption at $x/c = 0.6$ leads to a significant deviation of the shear stress at the top of the wall model.

For the wall modeling, we also have to consider the eddy-viscosity approximation for the total shear stress:

$$\mathcal{T}_{\xi\eta} = (\mu + \mu_{t,\mathrm{RANS}})\frac{d\overline{U}}{d\eta}, \tag{7}$$

where $\mu_{t,\mathrm{RANS}}$ is the RANS eddy viscosity. Note that the fluctuations of the density and molecular viscosity are neglected in the discussions below because the flow is almost incompressible and isothermal. The velocity profile and resulting the skin friction is accurately predicted only when both $\mathcal{T}_{\xi\eta}$ and $\mu_{t,\mathrm{RANS}}$ are properly modeled. In the existing equilibrium [14,39] and nonequilibrium [15,22] wall models, the mixing-length model

$$\mu_{t,\mathrm{RANS}} = \rho(\kappa\eta)\sqrt{\frac{\overline{\tau_w}}{\rho}}[1 - \exp(-\eta^+/17)]^2 \tag{8}$$

is used to approximate the RANS eddy viscosity. Here $\eta^+ \equiv \rho_w u_\tau \eta/\mu_w$, $u_\tau \equiv \sqrt{\overline{\tau_w}/\rho_w}$, and $\kappa = 0.41$. Also, another form of the mixing-length model [39,40] is written as

$$\mu_{t,\mathrm{RANS}} = \rho(\kappa\eta)^2\left|\frac{d\overline{U}}{d\eta}\right|[1 - \exp(-\eta^+/26)]^2. \tag{9}$$

An alternative modeling for the RANS eddy viscosity is derived based on the theoretical concept of the eddy viscosity [41]. Here the eddy viscosity is expressed as the product of the wall-normal velocity fluctuations and the mixing length $\kappa\eta$ as

$$\mu_{t,\mathrm{RANS}} = \rho(\kappa\eta)\sqrt{\overline{V'V'}}. \tag{10}$$

Figure 5 compares these eddy viscosity models to the effective RANS eddy viscosity of the WRLES data, which is calculated as

$$\mu_{t,\mathrm{RANS}} = \mathcal{T}_{\xi\eta}\left(\frac{d\overline{U}}{d\eta}\right)^{-1} - \mu. \tag{11}$$

The widely used mixing-length models [Eqs. (8) and (9)] tend to underestimate the eddy viscosity compared with Eq. (11), especially when the adverse pressure gradient is large ($x/c = 0.6$). On the

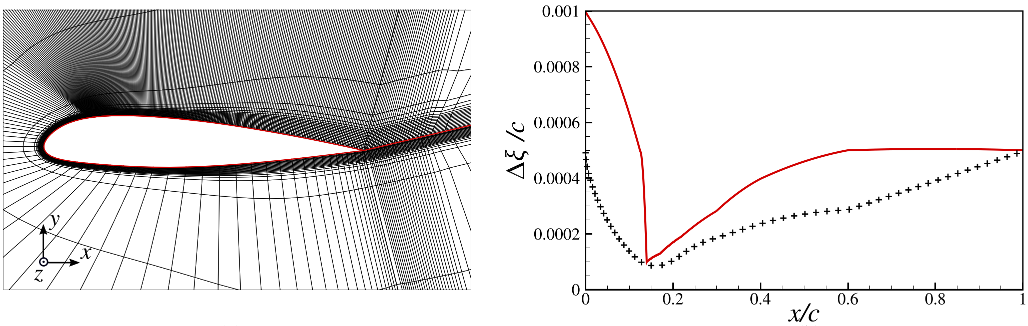

(a) (b)

FIG. 6. Computational grid for the WMLES. (a) Grid around the airfoil (every 10th grid points are shown). (b) Comparison of the chordwise grid spacing $\Delta\xi$ along the airfoil surface (——, WMLES; +, WRLES [4]).

other hand, Eq. (10) gives more accurate approximatioins of the eddy viscosity both at $x/c = 0.3$ and 0.6. The results suggest that $\sqrt{\overline{V'V'}}$ is strongly relevant to the eddy viscosity and that the adverse pressure gradient augments $\sqrt{\overline{V'V'}}$. Although $\sqrt{\overline{V'V'}}$ is not readily available during the simulation, further modeling of the eddy viscosity should be explored focusing on the wall-normal mixing of the turbulence.

III. PREDICTABILITY OF THE STALL PHENOMENA USING WALL-MODELED LES

In this section, we investigate the possibility and challenges for the WMLES for the prediction of the near-stall flowfield using WMLES. For this purpose, we conduct WMLES of the same flowfield as the WRLES as a numerical experiment. Here the wall-stress approach is employed and the equilibrium [14] and nonequilibrium [42] boundary layer (EQBL and NonEQBL) models are used to model τ_w. Note that the WMLES for this flowfield has already been conducted in the prior study [42]. However, the spanwise domain size (1.7%c) is not sufficient to remove the spurious correlation in the spanwise direction, following the observation by Asada and Kawai [4]. Therefore, in this study, we employ the same spanwise domain size with that in the previous WRLES (4.93%c).

A. Numerical settings of the wall-modeled LES

For the WMLES, a C-type computational grid [see Fig. 6(a)] is used. The number of the grid points for the WMLES is 3783 (chordwise) $\times$ 225 (wall-normal) $\times$ 297 (spanwise). In the chordwise direction, 2713, 350, and 360 grid points are located on the suction side, pressure side, and wake, respectively. The total number of grid points for the LES grid is 0.25 billion, which is approximately 5 times smaller than that of the reference WRLES [4] (1.2 billion grid points). The chordwise grid spacing in the region $x/c > 0.2$ is set to be approximately 1/25 of the local 99% boundary layer thickness δ_{99} based on the reference WRLES result [4]. The grid around the trailing edge is almost isotropic in the x-y plane ($\Delta x/c \approx \Delta y/c \approx 5.0 \times 10^{-4}$), and the grid is coarsened in the far wake region ($x/c > 1.2$). As shown in Fig. 6(b), the chordwise grid spacing of the WMLES grid is almost the same as that of the WRLES at the trailing edge and the transition location, and larger spacing in the other regions. The outer boundary of the computational grid r is set at 160c location, which is 8 times larger than that of the WRLES. We have confirmed that the difference in the outer boundary size slightly affects the suction peak near the leading edge but has almost no influence on the flow separation near the trailing edge (see Appendix). The spanwise domain size is set to the same size as the reference WRLES (4.93% c), and a periodic boundary condition is imposed at the spanwise boundaries. The spanwise grid size is 1/25 of the boundary layer thickness at $x/c = 0.2$ ($\Delta z/c = 1.66 \times 10^{-4}$), which is 2.4 larger grid size than that in the WRLES. Note that

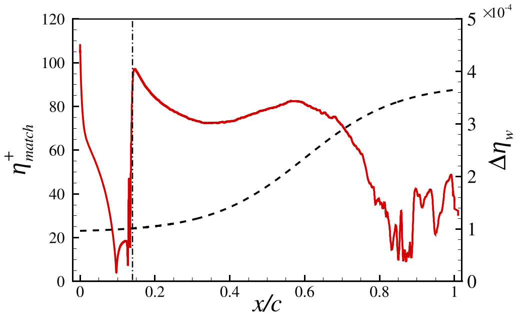

(a)

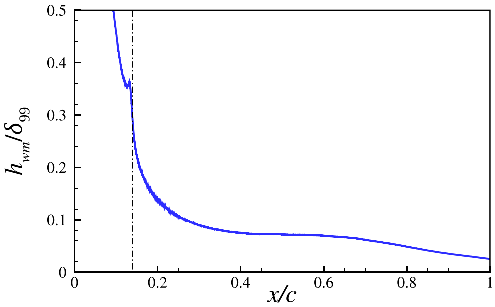

(b)

FIG. 7. Wall normal grid resolution: (a) - - -, grid spacing at the wall (using the right vertical axis); ——, η^+ at the matching location (using the left vertical axis). (b) Matching height h_{wm} relative to the 99% boundary layer thickness δ_{99}. The vertical dash-dotted line denotes the laminar-turbulent transition location ($x/c = 0.14$).

the wall-normal grid spacing is also set to smaller than $1/25$ of the local boundary layer thickness, which satisfies the proper WMLES criterion [6,14].

We adopt the fifth point from the wall ($\eta = h_{\mathrm{wm}}$) as the matching location, following the prior study [14]. In the WMLES, the matching location should be located within the log region ($\eta^+ > 50$). The skin friction decreases toward the turbulent separation point near the trailing edge, and thus, η^+ at the matching location also decreases if the wall-normal grid spacing is fixed. To maintain η^+ at the matching location to be within the log region, therefore, the wall-normal grid spacing at the wall $\Delta\eta_w$ is set to a variable of x/c; $\Delta\eta_w/c$ is 9.6×10^{-5} at the leading edge and increases to 3.7×10^{-4} at the trailing edge [see Fig. 7(a)]. The matching height h_{wm} is approximately $5\Delta\eta_w$, where the η^+ is shown in Fig. 7(a). Note that η^+ in this figure is calculated by using u_τ obtained by the reference WRLES result. Although the reduction of h^+_{wm} (η^+ at $\eta = h_{\mathrm{wm}}$) is inevitable near the turbulent separation point ($x/c \approx 0.85$), $h^+_{\mathrm{wm}} > 50$ is retained in $x/c < 0.6$, where the wall model is expected to be effective as discussed in Sec. II A. Also, we confirmed h_{wm} is set to the typical upper bound of the inner layer ($h_{\mathrm{wm}}/\delta_{99} < 0.1$) in $x/c > 0.27$, as shown in Fig. 7(b).

The SGS eddy viscosity for the LES is evaluated by the selective-mixed scale model [43]. The spatial derivatives in the LES and the NonEQBL model are evaluated by the sixth-order compact difference scheme [33], which is the same as the previous studies [14,15]. In addition, the eighth-order tridiagonal compact filter [36] is applied at each time step to eliminate numerical instability. In the LES, the time integration is conducted by the three-stage third-order total-variation-diminishing explicit Runge-Kutta method [44], whereas the time advancement in the NonEQBL model is evaluated by a second-order implicit time integration method [34,35] with five subiterations. The time-step size is set to $\Delta t u_\infty/c = 7.5 \times 10^{-6}$, which corresponds to the maximum Courant number of 0.69. The statistical data are obtained by averaging in the span direction and during the period $TU_\infty/c = 2.4$ after the flow reaches a quasisteady state. We have checked the statistical convergence of the flowfield and confirmed the velocity and Reynolds shear stress in the attached region ($x/c < 0.8$) almost does not change from those averaged over $TU_\infty/c = 1.2$.

In the WMLES, the wall-normal grid spacing near the wall boundary is relatively coarse, and the development of the very thin laminar boundary layer near the leading edge cannot be resolved sufficiently. The large skin friction imposed by the wall model causes flow reversal near the leading edge where the grid is too coarse compared with the boundary layer thickness, and consequently, the laminar-turbulent transition is induced artificially at an unexpected upstream location. To avoid the unintended transition to the turbulence, the flowfield upstream of the transition location ($x/c = 0.14$) is spatially filtered in the spanwise direction as $\hat{\mathbf{Q}}|_{I,J,K} = (\mathbf{Q}|_{I,J-1,K} + 2\mathbf{Q}|_{I,J,K} + \mathbf{Q}|_{I,J+1,K})/4$, where $\hat{\mathbf{Q}}$ is the filtered conservative variables, and subscripts I, J, and K are the chordwise, spanwise and wall-normal indexes of the grid, respectively. This

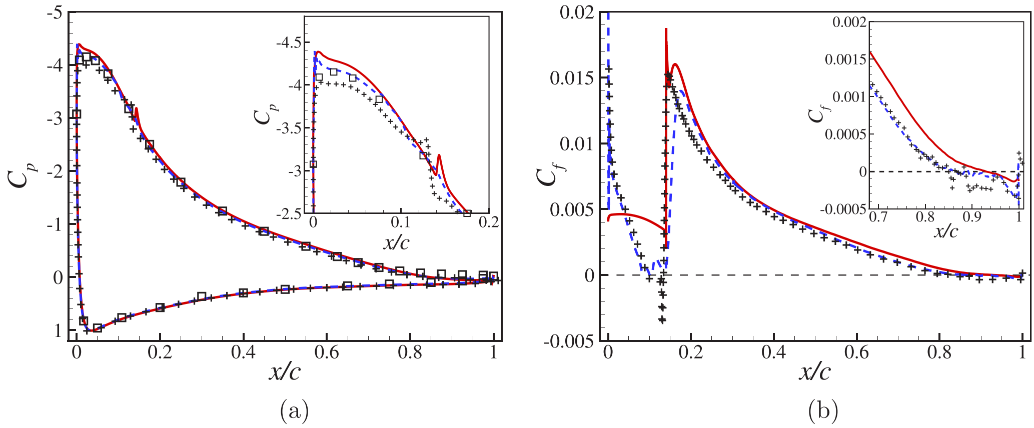

FIG. 8. Overall validity of the WMLES: (a) mean pressure coefficient and (b) skin friction coefficient (——, WMLES with the EQBL model; - - -, WMLES with the NonEQBL model; +, WRLES [4]; □, wind-tunnel experiment [45]).

spanwise filtering reduces the growth of the spanwise instability modes and retains the laminar flow in $x/c < 0.14$.

B. Overview of wall-modeled LES results

First, the overall accuracy and validity of the WMLES are addressed by comparing the results to the WRLES database. Figure 8 shows the time- and span-averaged pressure coefficient $C_p = 2(\overline{p} - p_\infty)/(\rho_\infty U_\infty^2)$ and the skin friction coefficient $C_f = 2\overline{\tau_w}/(\rho_\infty U_\infty^2)$ along the airfoil surface. Here the two WMLES show good agreement with the WRLES, except for the small difference in the suction peak. In the C_f distribution, the differences between the two WMLES results are more visible; the C_f peak near the leading edge due to the favorable pressure gradient is predicted only by the NonEQBL model. Furthermore, the flow separation location predicted by the NonEQBL model is close to the WRLES, while that by the EQBL model delays compared to the WRLES. Note that C_f obtained in the WMLES [Fig. 8(b)] indicates the skin friction imposed at the wall boundary of the LES, and the negative C_f value does not exactly mean the flow reversal in the LES. The ambiguity of the separation point can be confirmed in Fig. 9, where the probabilities of the negative skin friction and the flow reversal at the first WMLES grid point from the wall are shown. The negative skin friction obtained by the EQBL model indicates the flow reversal at the matching height, which is essentially different from the flow reversal at the first WMLES grid point from the wall. However, the ambiguity of the separation point does not influence the prediction of this flowfield because the skin friction near the separation point is not effective to the boundary layer development as discussed in Sec. II A.

To check the validity of the WMLES further, the velocity profiles, Reynolds shear-stress profiles, and the distribution of the momentum thickness are also compared in Fig. 10. The velocity and Reynolds shear-stress profiles and the boundary layer thickness in the WMLES with the NonEQBL model show good agreement with the WRLES. On the other hand, when the EQBL model is used, the boundary layer thickness is underestimated throughout the airfoil surface. The differences in the boundary layer thickness result in the difference of C_l because the displacement by the boundary layer at the trailing edge changes the circulation around the airfoil. The time-averaged C_l at $\alpha = 13.3^\circ$ obtained by the WMLES with the EQBL model ($C_l = 1.58$) and with the NonEQBL model ($C_l = 1.54$) are slightly higher than those of the WRLES ($C_l = 1.51$) and the experimental data ($C_l = 1.50$). Note that a part of the C_l discrepancy is caused by the different computational domain size. The computational domain size in the previous WRLES is $20c$, which is one-eighth

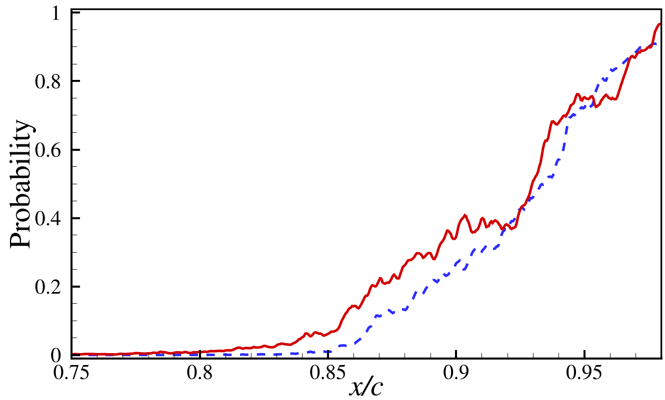

FIG. 9. Comparison of the probabilities of the flow reversal and negative skin friction (——, probability of flow reversal at the first WMLES grid point from the wall; - - -, probability of negative skin friction obtained by the EQBL model).

of the present WMLES. As shown in the Appendix, the C_l difference caused by the different computational domain sizes is approximately 0.02. By considering the effects of different domain sizes on C_l, WMLES with the NonEQBL model shows reasonable agreement with the WRLES, while the WMLES with the EQBL model still slightly overestimates the C_l.

Based on these results, we will discuss the following two points in the subsequent subsections. The first point is the accuracy of the wall models in the adverse pressure gradient locations. As discussed in Sec. II A, the skin friction in $0.2 < x/c < 0.6$ is important in the prediction of the stall phenomena. Here, we conduct the budget analysis presented in Sec. II B to understand the validity of the wall models. The second point is the causes of the different momentum thicknesses in the two WMLES. The integral-relation analysis (see Sec. II A) is conducted for these WMLES results, and we will discuss the predictability of the stall phenomena using the WMLES.

C. Behaviors of the wall models in the adverse pressure gradient region

The behaviors of the wall models in the adverse pressure gradient region are investigated to understand the validity of the wall models in that region. To evaluate the strength of the pressure gradient in the inner layer of the turbulent boundary layer, the wall-scale pressure gradient parameter [46] P^+ is introduced. The definition of P^+ is

$$P^+ \equiv \nu_w \frac{d\overline{p}}{d\xi} / \left(\overline{\rho_w} u_\tau^3\right), \tag{12}$$

where ν_w is the kinematic viscosity at the wall. Figure 11 compares the velocity profile in the wall model to the WRLES at $P^+ = 0.0062$ and $P^+ = 0.017$. Note that these locations corresponds to $x/c = 0.3$ and 0.6 in the WRLES (see Figs. 4 and 5), respectively, and the Clauser parameter [47] $\beta = [\delta^*/\overline{\tau_w}(dP/d\xi)]$ is also almost the same among the three cases ($0.96 < \beta < 1.04$ at $P^+ = 0.0062$ and $5.4 < \beta < 5.9$ at $P^+ = 0.017$). When the pressure gradient is small ($P^+ = 0.0062$), the velocity profile obtained by the two wall model collapses. At the larger pressure gradient location ($P^+ = 0.017$), U^+ obtained by the WRLES deviate lower from the log-law profile. Here, the EQBL model retains the same velocity profile as that at $P^+ = 0.0062$, while the NonEQBL model slightly overpredicts the U^+ at the top.

The causes of the different behaviors of the wall models at $P^+ = 0.017$ are investigated through the budget analysis described in Sec. II B to understand the applicability of the wall models. Figures 12 and 13 show the total shear stress [Eq. (6)] and effective RANS eddy viscosity [Eq. (11)] profiles in the wall models, respectively. The NonEQBL model predicts the total shear stress profile

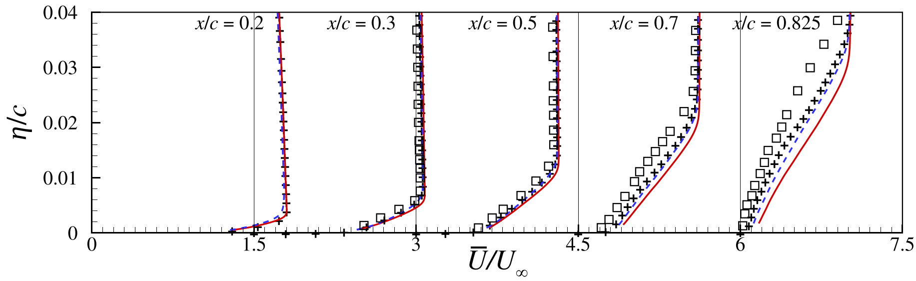

(a) Mean velocity profiles (Each profiles is separated by a horizontal offset of 1.5)

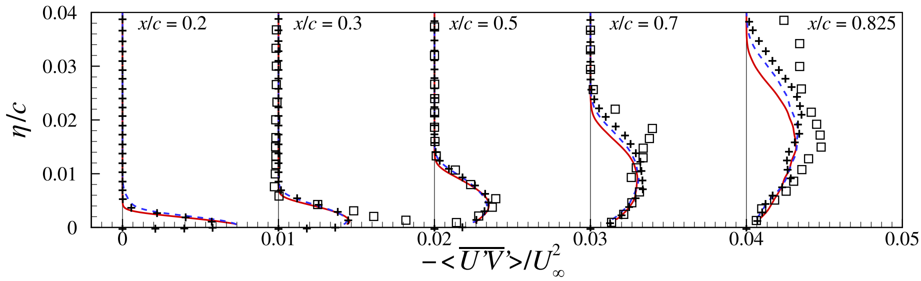

(b) Reynolds shear-stress profiles (Each profiles is separated by a horizontal offset of 0.01)

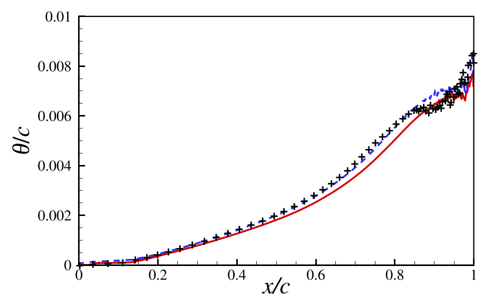

(c) Distributions of the momentum thickness

FIG. 10. Development of the boundary layer along the airfoil upper surface. Lines and symbols are as in Fig. 8.

accurately because the NonEQBL model includes the convection and pressure gradient terms, while the effective RANS eddy viscosity in the NonEQBL model is underestimated compared to the WRLES. This underestimation of the eddy viscosity is because the NonEQBL model employs the mixing-length model [Eq. (8)] for the baseline RANS eddy viscosity, although the NonEQBL model also uses the dynamic damping procedure [15] to consider the resolved Reynolds stress. As shown in Fig. 5, Eq. (8) tends to underestimate the effective eddy viscosity in the adverse pressure gradient region. The underestimation of the eddy viscosity consequently leads to the discrepancy of the velocity at the top of the wall model [see Fig. 11(b)]. These results indicate that the eddy viscosity model used in the wall model must reflect the nonequilibrium effects in the boundary layer to retain consistency with the total shear stress. On the other hand, the EQBL model always assumes a constant shear stress distribution in the wall-normal direction as its nature, and thus the total shear stress is underestimated compared to the WRLES. The eddy viscosity is also underestimated as shown in Fig. 5, and, consequently, the velocity profiles and the resulting C_f obtained by the EQBL

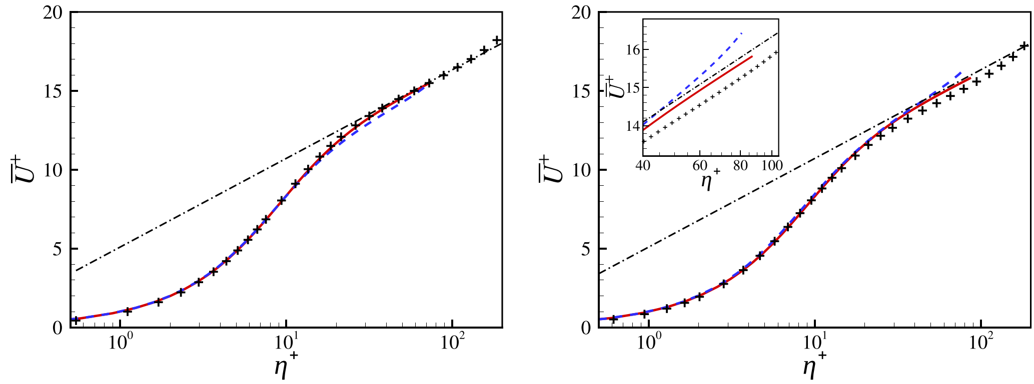

(a) $P^+ = 0.0065$ $(x/c \approx 0.3)$ (b) $P^+ = 0.017$ $(x/c \approx 0.6)$

FIG. 11. Nondimensional velocity profile in the wall unit. The black dash-dotted line shows the log-law $u^+ = \log(\eta^+)/0.41 + 5.1$, and the other lines and symbols are as in Fig. 8.

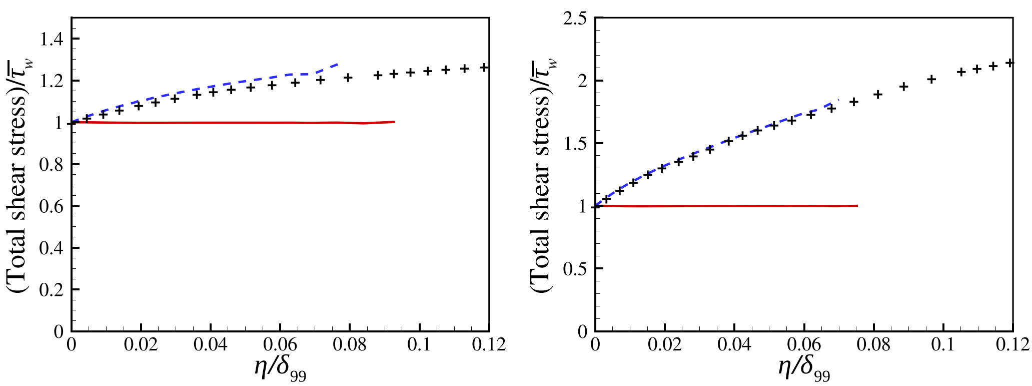

(a) $P^+ = 0.0065$ $(x/c \approx 0.3)$ (b) $P^+ = 0.017$ $(x/c \approx 0.6)$

FIG. 12. Total shear stress in the wall model. The lines and symbols are as in Fig. 8.

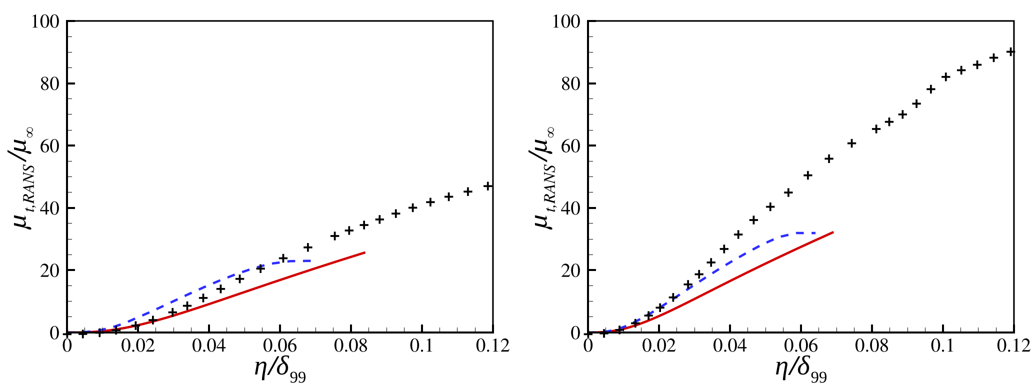

(a) $P^+ = 0.0065$ $(x/c \approx 0.3)$ (b) $P^+ = 0.017$ $(x/c \approx 0.6)$

FIG. 13. Effective eddy viscosity profile in the wall models. The lines and symbols are as in Fig. 8.

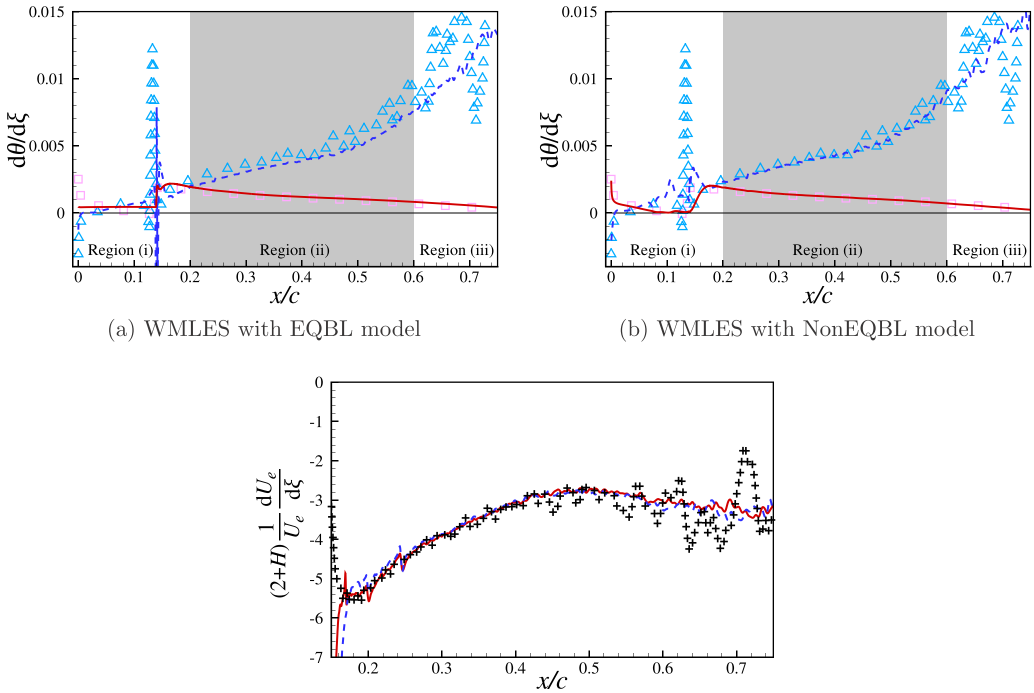

(a) WMLES with EQBL model

(b) WMLES with NonEQBL model

(c) Comparison of II/θ (lines and symbols as in Fig. 8)

FIG. 14. Integral relation using the WMLES results (——, I; - - -, II. The WRLES result is also plotted with symbols (□, I; △, II).

model does not deviate far from the WRLES result. However, the coincidence of the velocity profiles at these locations does not assure the global applicability of the EQBL model for nonequilibrium flows because both the total stress and the eddy viscosity are inconsistent with the observations from the WRLES. Vinuesa *et al.* [48] reported the intercept of the log-law in adverse pressure gradient boundary layer is influenced by the history of the upstream boundary layer. The EQBL model cannot predict the deviation from the assumed log-law velocity profile, and therefore, the nonequilibrium effects should be properly modeled to improve the applicability of the wall model to complex flows.

D. Predictability of trailing-edge stall using wall-modeled LES

Here, the predictability of the trailing-edge stall phenomena using the WMLES is discussed through the integral relation analysis [Eq. (1)]. Figures 14(a) and 14(b) show the terms of Eq. (1) in the WMLES results. I and II in the WMLES with the NonEQBL model are in good agreement with those in the WRLES data in region (ii) and (iii), while that with the EQBL model underestimates II. The underestimation of II when the EQBL model is used is because the momentum thickness at $x/c = 0.2$ is underestimated when the EQBL model is used [see Fig. 8(c)]. The difference of II is clearly due to the difference of θ itself because the rest of II is almost the same among the two WMLES and WRLES, as shown in Fig. 14(c).

By considering the effects of the difference in θ at $x/c = 0.2$, the boundary layer development in regions (ii) and (iii) predicted by the two WMLES shows reasonable agreement with the WRLES. The accuracy of the WMLES in regions (ii) and (iii) is due to the following two reasons:

(i) I, the effects of the skin friction obtained by the wall model, is effective only in $x/c < 0.6$. Despite the potential problems stated in Sec. III C, the equilibrium and the nonequilibrium wall models have reasonable accuracy in region (ii) (see Fig. 11).

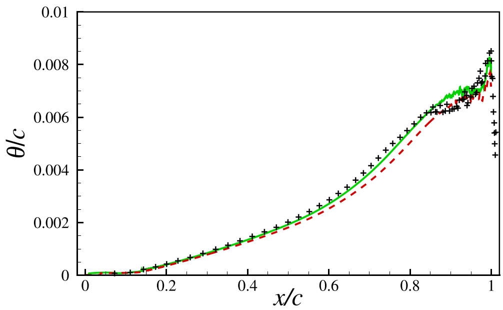

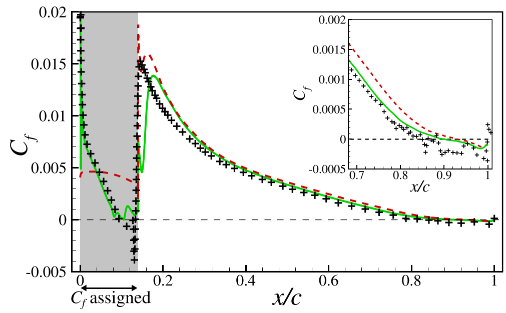

FIG. 15. Influences of the difference in skin friction near the leading edge on the WMLES. (a) momentum thickness and (b) skin friction coefficient near the trailing edge (——, Case A; - - -, WMLES with EQBL model; +, WRLES).

(ii) II has larger contributions to the development of the momentum thickness than I in regions (ii) and (iii). In the WMLES, the outer layer turbulence is sufficiently resolved, and thus, the prediction of II is essentially accurate given that θ at that place (i.e., the accumulation of the upstream history) is correct.

Therefore, the results suggest that the boundary layer development can be predicted accurately by the WMLES once the boundary layer thickness at the upstream boundary of region (ii) ($x/c = 0.2$) is correct.

To understand the predictability of the stall phenomena, the prediction of the θ near the leading edge should also be addressed. One of the causes of the different θ at $x/c = 0.2$ is the I (i.e., C_f) near the leading edge. To quantify the effects of I near the leading edge, we conduct a numerical experiment as follows. Here the time- and span-averaged C_f in the WMLES with the NonEQBL model is imposed before the transition location ($x/c = 0.14$) instead of τ_w calculated by the EQBL model, and the EQBL model is solved only downstream of the transition location. Figure 15 shows the streamwise development of θ and the distributions of C_f near the trailing edge obtained by this computational set-up (denoted as Case A). The momentum thickness increases throughout the airfoil surface, and the separation point moves upstream. Related to the move of the separation point, C_l decreases by 0.06 ($C_l = 1.52$) compared to the original WMLES result using the EQBL model. This numerical experiment indicates that the difference in the laminar part affects the downstream region. Also, II is not predicted accurately in the laminar-turbulent transition location ($0.1 < x/c < 0.2$) because the grid used here is not fine enough to resolve the thin boundary layer. The underresolution near the leading edge is a consistent problem for the WMLES framework using the quantities at points away from the wall, which should be considered in the future to further improve the predictability of the trailing edge stall phenomena.

IV. CONCLUSIONS

In this research, we analyzed the flowfield around the A-airfoil at the near-stall condition that was obtained by the prior WRLES [4] to understand the mechanism of the boundary layer development and to examine the predictability of the trailing-edge stall phenomena using the WMLES. The analysis based on the integral relation for the boundary layer reveals that the skin friction is effective to the boundary layer development only in the turbulent region with a mild-adverse pressure gradient ($0.2 < x/c < 0.6$) and in the laminar region near the leading edge ($x/c < 0.05$), while the effects of the deceleration of the flow outside the boundary layer are dominant near the turbulent separation point. The effects of the skin friction accumulates along the airfoil surface, and thus, the skin friction in the upstream region ($x/c < 0.6$) is important for the prediction of the boundary layer development and the consequent flow separation near the trailing edge. Also, the skin friction in $x/c > 0.6$ is not effective to the boundary layer development, which suggests and accurate wall modeling is not necessarily required near and downstream of the separation location ($x/c > 0.6$). Then, the inner layer turbulence modeling is investigated in the mild-adverse pressure gradient region ($0.2 < x/c < 0.6$). The budget analysis indicates that the total shear stress increases in the wall-normal direction due to the nonequilibrium effects (i.e., contributions of the convection and pressure gradient terms). In addition to the shear stress, the effective RANS eddy viscosity in the boundary layer also increases from the equilibrium condition. This trend of the eddy viscosity cannot be reproduced by the conventional mixing-length models, which suggests the necessity of alternative modeling for the eddy viscosity for the nonequilibrium wall models.

In the WMLES, the overall accuracy of the predicted mean flowfield (e.g., C_p) was reasonable. This is because the development of the boundary layer near the flow separation is mostly due to the outer-layer turbulence, as indicated in the integral-relation analysis presented in Sec. III D. The energetic vortices in the outer layer of the boundary layer are sufficiently resolved in the WMLES, which is a great advantage in predicting the stall phenomena. The WMLES results also suggest the following two points that should be addressed to further improve the accuracy and global applicability of the WMLES. The first point is that the eddy viscosity model in the wall must be modified from that of the equilibrium wall model if the nonequilibrium effects are included. The adverse pressure gradient augments the eddy viscosity, and thus, the velocity gradient in the wall model tends to be overestimated if the original eddy viscosity model is used. The second point is that the thin laminar boundary layer near the leading edge has nonnegligible effects on the development of the downstream boundary layer. The treatment for the underresolved boundary layer near the leading edge including the modeling of the laminar-turbulent transition should be a future challenging problem for the WMLES.

ACKNOWLEDGMENTS

This work was supported in part by MEXT as Program for Promoting Researches on the Supercomputer Fugaku (Leading research on innovative aircraft design technologies to replace flight test) and the former Social and Scientific Priority Issue (Development of innovative design and production processes that lead the way for the manufacturing industry in the near future) to be tackled by using post-K computer. A part of this research uses computational resources of the K computer provided by the RIKEN Advanced Institute for Computational Science (Project ID: hp150254, hp160205, hp170267, hp180185, hp190164). We also acknowledge Dr. H. Bezard for providing the experimental data and Dr. K. Asada for the WRLES data.

APPENDIX: EFFECTS OF OUTER DOMAIN SIZE

The outer boundary of the reference WRLES [4] is set $20c$ away from the leading edge of the airfoil. In the WMLES in this study, we set the outer boundary size $r = 160c$ because a small outer boundary size may affect the flow around the airfoil. WMLES with the same domain size as the reference WRLES ($r = 20c$) is therefore computed to evaluate the effects of the outer boundary size. Here, we compare the results using the EQBL model. The computational grid has 3743 (chord) $\times$ 205 (wall-normal) $\times$ 297 (span) grid points, where only the outer part of the computational domain is changed.

Figure 16(a) shows the distributions of the mean pressure coefficient on the airfoil. When the outer boundary size is small, the suction peak is slightly reduced. Consequently, the time-averaged C_l becomes 1.56, which is 0.02 lower than the result with the larger outer boundary size. This difference suggests that the outer boundary of the reference WRLES is not sufficiently large to consider the outer boundary as the free stream. Nevertheless, almost no difference is observed in the skin friction coefficient near the trailing edge, as shown in Fig. 16(b). Therefore, we conclude that

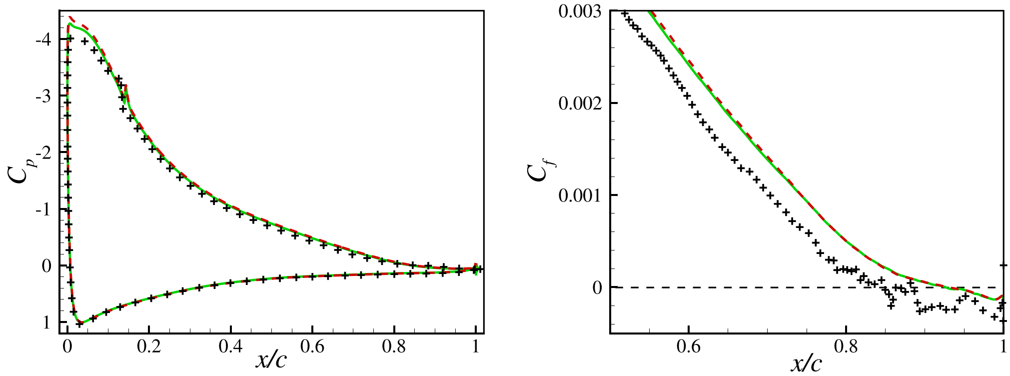

(a) Pressure coefficient (b) Skin friction coefficient near the trailing edge

FIG. 16. Influences of the outer domain size on the mean pressure coefficient and skin friction coefficient along the airfoil [- - -, WMLES (EQBL) with $r = 160c$; ——, WMLES (EQBL) with $r = 20c$; +, WRLES [4] with $r = 20c$].

we may compare the WMLES and the reference WRLES results in terms of the physics of the flow separation although the outer boundary size is different.

---

[1] D. E. Gault, A correlation of low-speed, airfoil-section stalling characteristics with Reynolds number and airfoil geometry, Techical Report NASA-TM 3963 (National Aeronautics and Space Administration, Washington, DC, 1957).

[2] I. Tani, Low-speed flows involving bubble separations, Prog. Aeronaut. Sci. **5**, 70 (1964).

[3] I. Mary and P. Sagaut, Large eddy simulation of flow around an airfoil near stall, AIAA J. **40**, 1139 (2002).

[4] K. Asada and S. Kawai, Large-eddy simulation of airfoil flow near stall condition at Reynolds number 2.1×10^6, Phys. Fluids **30**, 085103 (2018).

[5] LES database, http://www.klab.mech.tohoku.ac.jp/database/.

[6] D. R. Chapman, Computational aerodynamics development and outlook, AIAA J. **17**, 1293 (1979).

[7] H. Choi and P. Moin, Grid-point requirements for large eddy simulation: Chapmans estimates revisited, Phys. Fluids **24**, 011702 (2012).

[8] U. Piomelli and E. Balaras, Wall-layer models for large-eddy simulations, Annu. Rev. Fluid Mech. **34**, 349 (2002).

[9] J. Larsson, S. Kawai, J. Bodart, and I. Bermejo-Moreno, Large eddy simulation with modeled wall-stress: Recent progress and future directions, Mech. Eng. Rev. **3**, 15-00418 (2016).

[10] S. T. Bose and G. I. Park, Wall-modeled large-eddy simulation for complex turbulent flows, Annu. Rev. Fluid Mech. **50**, 535 (2018).

[11] M. L. Shur, P. R. Spalart, M. K. Strelets, and A. K. Travin, A hybrid RANS-LES approach with delayed-DES and wall-modelled LES capabilities, Int. J. Heat Fluid Flow **29**, 1638 (2008).

[12] J. W. Deardorff, A numerical study of three-dimensional turbulent channel flow at large Reynolds numbers, J. Fluid Mech. **41**, 453 (1970).

[13] M. Wang and P. Moin, Dynamic wall modeling for large-eddy simulation of complex turbulent flows, Phys. Fluids **14**, 2043 (2002).

[14] S. Kawai and J. Larsson, Wall-modeling in large eddy simulation: Length scales, grid resolution, and accuracy, Phys. Fluids **24**, 015105 (2012).

[15] S. Kawai and J. Larsson, Dynamic non-equilibrium wall-modeling for large eddy simulation at high Reynolds numbers, Phys. Fluids **25**, 015105 (2013).

[16] Z. L. Chen, S. Hickel, A. Devesa, J. Berland, and N. A. Adams, Wall modeling for implicit large-eddy simulation and immersed-interface methods, Theor. Comput. Fluid Dyn. **28**, 1 (2014).

[17] G. I. Park and P. Moin, An improved dynamic non-equilibrium wall-model for large eddy simulation, Phys. Fluids **26**, 015108 (2014).

[18] D. Chung and D. Pullin, Large-eddy simulation and wall modeling of turbulent channel flow, J. Fluid Mech. **631**, 281 (2009).

[19] S. Bose and P. Moin, A dynamic slip boundary condition for wall-modeled large-eddy simulation, Phys. Fluids **26**, 015104 (2014).

[20] H. J. Bae, A. Lozano-Durán, S. T. Bose, and P. Moin, Dynamic slip wall model for large-eddy simulation, J. Fluid Mech. **859**, 400 (2019).

[21] X. Yang, J. Sadique, R. Mittal, and C. Meneveau, Integral wall model for large eddy simulations of wall-bounded turbulent flows, Phys. Fluids **27**, 025112 (2015).

[22] S. Hickel, E. Touber, J. Bodart, and J. Larsson, A parametrized non-equilibrium wall-model for large-eddy simulations, in *Proceedings of the Summer Program, Center for Turbulence Research* (Stanford University, Stanford, 2012), p. 127.

[23] A. Avdis, S. Lardeau, and M. Leschziner, Large eddy simulation of separated flow over a two-dimensional hump with and without control by means of a synthetic slot-jet, Flow, Turbul. Combust. **83**, 343 (2009).

[24] P. Balakumar, G. Park, and B. Pierce, DNS, LES, and wall-modeled LES of separating flow over periodic hills, in *Proceedings of the Summer Program* (Stanford University, Stanford, 2014), pp. 407–415.

[25] P. S. Iyer and M. R. Malik, Wall–modeled large eddy simulation of flow over a wall–mounted hump, in *Proceedings of the 46th AIAA Fluid Dynamics Conference, Washington, DC, 2016* (AIAA, Reston, 2016), paper 2016–3186.

[26] G. I. Park, Wall-modeled large-eddy simulation of a high Reynolds number separating and reattaching flow, AIAA J. **55**, 3709 (2017).

[27] O. Lehmkuhl, G. Park, S. Bose, and P. Moin, Large-eddy simulation of practical aeronautical flows at stall conditions, in *Proceedings of the 2016 Summer Program, Center for Turbulence Research* (Stanford University, Stanford, 2018).

[28] S. Kawai and J. Larsson, A non-equilibrium wall-model for LES of shock/boundary layer interaction at high reynolds number, in *Proceedings of the 42nd AIAA Fluid Dynamics Conference and Exhibit, New Orleans, 2012* (AIAA, Reston, 2012), paper 2012–2976.

[29] I. Bermejo-Moreno, L. Campo, J. Larsson, J. Bodart, D. Helmer, and J. K. Eaton, Confinement effects in shock wave/turbulent boundary layer interactions through wall-modelled large-eddy simulations, J. Fluid Mech. **758**, 5 (2014).

[30] Y. Fukushima and S. Kawai, Wall-modeled large-eddy simulation of transonic airfoil buffet at high Reynolds number, AIAA J. **56**, 2372 (2018).

[31] T. Von Kármán, Uber laminare und turbulente reibung, Z. Angew. Math. Mech. **1**, 233 (1921) (in German).

[32] S. Kawai and K. Fujii, Compact scheme with filtering for large-eddy simulation of transitional boundary layer, AIAA J. **46**, 690 (2008).

[33] S. K. Lele, Compact finite difference schemes with spectral-like resolution, J. Comput. Phys. **103**, 16 (1992).

[34] S. Obayashi, K. Fujii, and S. Gavali, Navier–Stokes simulation of wind-tunnel flow using LU-ADI factorization algorithm, Technical Report NASA-TM 10004 (National Aeronautics and Space Administration, Washington, DC, 1988).

[35] N. Izuka, Study of mach number effect on the dynamic stability of a blunt re-entry capsule, Ph.D. thesis, The University of Tokyo, 2006.

[36] D. V. Gaitonde and M. R. Visbal, Padé-type higher-order boundary filters for the Navier–Stokes equations, AIAA J. **38**, 2103 (2000).

[37] M. Drela, Xfoil: An analysis and design system for low Reynolds number airfoils, in *Low Reynolds Number Aerodynamics* (Springer, Berlin, 1989), pp. 1–12.

[38] G. Coleman, C. Rumsey, and P. Spalart, Numerical study of turbulent separation bubbles with varying pressure gradient and Reynolds number, J. Fluid Mech. **847**, 28 (2018).

[39] P. S. Iyer and M. R. Malik, Analysis of the equilibrium wall model for high-speed turbulent flows, Phys. Rev. Fluids **4**, 074604 (2019).
[40] B. Baldwin and H. Lomax, Thin-layer approximation and algebraic model for separated turbulent flows, in *Proceedings of the 16th Aerospace Sciences Meeting, Huntsville, 1978* (AIAA, Reston, 1978), paper 78–0257.
[41] H. Tennekes and J. L. Lumley, *A First Course in Turbulence* (MIT Press, Cambridge, MA, 1972).
[42] S. Kawai and K. Asada, Wall-modeled large-eddy simulation of high Reynolds number flow around an airfoil near stall condition, Comput. Fluids **85**, 105 (2013).
[43] E. Lenormand, P. Sagaut, L. T. Phuoc, and P. Comte, Subgrid-scale models for large-eddy simulations of compressible wall bounded flows, AIAA J. **38**, 1340 (2000).
[44] S. Gottlieb and C.-W. Shu, Total variation diminishing Runge-Kutta schemes, Math. Comput. Am. Math. Soc. **67**, 73 (1998).
[45] C. Gleyzes and P. Capbern, Experimental study of two AIRBUS/ONERA airfoils in near stall conditions. Part I: Boundary layers, Aerosp. Sci. Technol. **7**, 439 (2003).
[46] T. Knopp, T. Alrutz, and D. Schwamborn, A grid and flow adaptive wall-function method for RANS turbulence modelling, J. Comput. Phys. **220**, 19 (2006).
[47] F. H. Clauser, Turbulent boundary layers in adverse pressure gradients, J. Aeronaut. Sci. **21**, 91 (1954).
[48] R. Vinuesa, P. S. Negi, M. Atzori, A. Hanifi, D. S. Henningson, and P. Schlatter, Turbulent boundary layers around wing sections up to rec = 1,000,000, Int. J. Heat Fluid Flow **72**, 86 (2018).

Correction: A minus sign was missing in Eq. (1) and has been inserted. The previously published Figure 10(b) contained an axis-label error and has been replaced.